



## Open Archive TOULOUSE Archive Ouverte (OATAO)

OATAO is an open access repository that collects the work of Toulouse researchers and makes it freely available over the web where possible.

This is an author-deposited version published in : <http://oatao.univ-toulouse.fr/>  
Eprints ID : 5675

To link to this article : DOI: 10.1016/j.ces.2011.10.067  
URL : <http://dx.doi.org/10.1016/j.ces.2011.10.067>

To cite this version :

Maniero, Riccardo and Climent, Eric and Bacchin, Patrice  
*Adhesion and detachment fluxes of micro-particles from a permeable wall under turbulent flow conditions*. (2012) Chemical Engineering Science, vol. 71, pp. 409-421. ISSN 0009-2509

Any correspondence concerning this service should be sent to the repository administrator: [staff-oatao@listes.diff.inp-toulouse.fr](mailto:staff-oatao@listes.diff.inp-toulouse.fr)

# Adhesion and detachment fluxes of micro-particles from a permeable wall under turbulent flow conditions

Riccardo Maniero<sup>a,c</sup>, Eric Climent<sup>b,c,\*</sup>, Patrice Bacchin<sup>a,c</sup>

<sup>a</sup> Université de Toulouse, INPT-UPS, Laboratoire de Génie Chimique 4 Allée Emile Monso, F 31432 Toulouse, France

<sup>b</sup> Université de Toulouse, INPT-UPS, Institut de Mécanique des Fluides Rue Camille Soula, F 31400 Toulouse, France

<sup>c</sup> CNRS, Fédération de recherche FERMAT, Toulouse, France

## A B S T R A C T

We report a numerical investigation of the deposition and re-entrainment of Brownian particles from a permeable plane wall. The tangential flow was turbulent. The suspension dynamics were obtained through direct numerical simulation of the Navier–Stokes equations coupled to the Lagrangian tracking of individual particles. Physical phenomena acting on the particles such as flow transport, adhesion, detachment and re-entrainment were considered. Brownian diffusion was accounted for in the trajectory computations by a stochastic model specifically adapted for use in the vicinity of the wall. Interactions between the particles and the wall such as adhesion forces and detachment were modeled. Validations of analytical solutions for simplified cases and comparisons with theoretical predictions are presented as well. Results are discussed focusing on the interplay between the distinct mechanisms occurring in the fouling of filtration devices. Particulate fluxes towards and away from the permeable wall are analyzed under different adhesion strengths.

## Keywords:

Colloidal dispersion  
Dynamic simulation  
Hydrodynamics  
Mass transfer  
Particles  
Turbulence

## 1. Introduction

The Physics of transport, deposition, detachment and re-entrainment of colloidal particles suspended in a fluid are of great interest in many areas of fluid engineering: fouling of heat exchangers, contamination of nuclear reactors, plugging of filtration membranes, occlusion of human veins, and deposits in microelectronics and paper industries. Although many models have been developed to predict these particular phenomena occurring in industrial applications, we are still far from a comprehensive description of the interplay between all the physical–chemical mechanisms. The aim of this work is to investigate the effect of hydrodynamics on the deposition of Brownian particles, more specifically turbulence effects.

Various theoretical models have been proposed to predict particle deposition onto a surface under laminar and turbulent regimes. Regarding laminar flows, (Bowen et al., 1976; Bowen and Epstein, 1979) proposed a combined transport and adhesion model based on the particle/wall interaction forces. Later, Adomeit and Renz (1996) and Yiantsios and Karabelas (2003) collected experimental data and developed a Eulerian approach combining physical–chemical and fluid dynamics aspects to predict the rate of deposition onto smooth surfaces under laminar flow.

This approach assumes constitutive equations to model the Lagrangian nature of the particle trajectories by transport and diffusion fluxes towards the wall supplemented by non-hydrodynamic particle/wall interactions. Preserving the Lagrangian nature of the dispersed phase, Kim and Zydney (2004) examined the particle trajectories in laminar cross-flow filtration accounting for electrostatic, hydrodynamic and Brownian contributions. These authors show the importance of repulsive effects in the transport of particles towards the surface. However, these simulations are limited to laminar flow conditions.

The flow regime in a filtration system is a crucial aspect of the process operation. Actually, most industrial processes are carried out under turbulent flow conditions: turbulence reduces the buildup of the particulate boundary layer due to hydrodynamic dispersion. But, the lack of proper theoretical modeling depicting the effect of turbulence on mass transport phenomena renders the prediction of fouling conditions mostly empirical. Most fouling simulation in turbulent regime relies on the balance between the dispersive mass transport phenomena (e.g. diffusion, lateral migration, shear-induced diffusion, colloidal interaction) and the permeate flux in an estimated boundary layer. These simulations do not account for the spatial and temporal heterogeneities in mass transport locally induced by turbulence. For example, these local heterogeneities could be a cause of the distribution in critical flux, which has been pointed out (Bacchin et al., 2005) to explain the discrepancies between experiment and simulation. Indeed, there is still a lack of predictive models able to simultaneously consider all these phenomena and their interactions under turbulent flow conditions.

\* Correspondence to: Institut de Mécanique des Fluides de Toulouse, CNRS-INPT-UPS 1, Allée du Prof. Camille Soula, F-31400 Toulouse, France.  
E-mail address: climent@imft.fr (E. Climent).

Early models of particle deposition onto a smooth surface were based on the concept of “stopping distance” (Davies, 1966; Sehmel, 1970). When particles embedded in the viscous sublayer reach this “stopping distance”, collision with the wall is considered. Cleaver and Yates (1975) showed that large discrepancies between prediction based on this concept and experimental data may occur under turbulent flow regime. Consequently, they complemented the theory accounting for the presence of sweep flows towards the wall. Dabros and Van de Ven (1983) derived an advection/diffusion equation describing mass transfer in the viscous sublayer for particles of negligible inertia. Based on comparisons with experiment, they found a better agreement with their downsweep model than the classic “stopping distance” approach. Similarly, Lai and Nazaroff (2000) account for the driving force of buoyancy supplemented with Brownian and turbulent diffusion. They showed that distinct regimes of impaction can be distinguished depending on the size and inertia of the particles, and turbulent flow conditions.

Nowadays, the turbulence (at moderate Reynolds numbers) can be fully resolved by Direct Numerical Simulation (DNS) and can capture the dynamic effects on the adhesion of particles in simplified geometries. DNS coupled to Lagrangian particle tracking have been applied to obtain detailed information on particle wall interactions for turbulent duct flow. Marchioli et al. (2003) analyzed the role of turbulence on particle transfer for circular vertical pipes. They also discussed the tight relationship between inertial migration in the boundary layer and the impaction rate. The case of inertial particles is specific while particle dynamics is controlled by flow structures with a time scale comparable to the particulate relaxation time. With sub-micronic particles (no inertia) embedded in a turbulent flow, Brownian diffusion prevails in the viscous sublayer (Shams et al., 2000).

Following the original work of Zhang and Ahmadi (2000), our aim was to simulate the transport of Brownian particles based on a Eulerian–Lagrangian approach including deposition, detachment and re-entrainment of the particles suspended in a fluid flowing under a turbulent regime. We compared our results to models based on convection/diffusion equations developed to predict fouling in laminar (Song and Elimelech, 1995) or turbulent (Minnikanti et al., 1999) conditions.

Compared to current applications, various assumptions will be made: e.g. dilute particle dispersion, absence of electric double layer repulsion, simple geometry. We focused our modeling approach on specific aspects: Direct Numerical Simulation (DNS) to determine the flow field and the wall shear stress, “optimal stopping” for predicting Lagrangian tracking in the vicinity of the wall, and Van der Waals adhesion forces using the Johnson–Kendall–Roberts (1971) model of adhesion and detachment.

## 2. Description of flow simulations

The study is based on the full resolution of turbulent flow in a simplified geometry (see Fig. 1). The typical length and velocity scales refer to cross-flow filtration in a tubular ceramic or polymeric membrane (typical diameter varies between  $D=1$  mm

and 1 cm). A very dilute (typically 0.1% volumetric concentration) suspension of micro-particles flows within this tube with a bulk tangential velocity  $\langle \bar{u} \rangle$  of around 1 m/s. In terms of dimensionless numbers, the flow regime is characterized by Reynolds number  $Re = \langle \bar{u} \rangle D / \nu$  equal to 4000 when  $D=4$  mm and the kinematic viscosity  $\nu=10^{-6}$  m<sup>2</sup>/s for water. This means that such operating conditions of cross-flow filtration correspond to moderately turbulent flow. The permeation flux is characterized by a wall normal velocity  $u_w$  typically on the order of  $10^{-5}$  m/s yielding  $u_w / \langle \bar{u} \rangle \sim 10^{-5}$ . In this range of permeable flux, we do not expect any modification of the turbulent flow structure due to the presence of the cross-flow (only minor effects on the wall shear stress have been observed by Hanh et al. (2002) for values of the filtration flux at least two orders of magnitude larger than ours).

Direct Numerical Simulation (DNS) is based on fully resolved solution of the Navier–Stokes equations regarding all the scales of turbulent flow (full resolution of local and temporal flow structures from the large-scale motions down to the Kolmogorov scale). The fluid is considered Newtonian and incompressible with constant physical properties ( $\rho$  is the fluid density and  $\mu$  its dynamic viscosity). The unsteady three-dimensional Navier–Stokes Eq. (1(a)–(b)) are solved on a Cartesian grid for a channel configuration.

$$\nabla \cdot \mathbf{u} = 0 \quad (1a)$$

$$\rho \left( \frac{\partial \mathbf{u}}{\partial t} + \nabla \mathbf{u} \mathbf{u} \right) = -\nabla P + \nabla [\mu (\nabla \mathbf{u} + \nabla^T \mathbf{u})] \quad (1b)$$

These equations are solved using a conservative finite-volume method. Primitive variables (velocity  $\mathbf{u}$  and pressure  $P$ ) are located on a staggered non-uniform Cartesian grid. Spatial derivatives are computed with second-order accuracy. Temporal integration is achieved through a third-order Runge–Kutta scheme and a semi-implicit Crank–Nicholson scheme for the viscous term. The incompressibility of the flow is achieved using an auxiliary potential for the projection method leading to a Poisson equation for pressure correction. The convergence criterion is fixed to  $10^{-8}$ , which permits to account precisely for fluid velocity as small as  $u_w \sim 10^{-5}$ . The corresponding simulation code, named JADIM, has been widely used and validated under laminar and turbulent flow regimes using either direct numerical simulation or large eddy simulations for higher Reynolds turbulence (e.g. Calmet and Magnaudet (2003), Climent and Magnaudet (2006) and references therein). In our study no sub-grid modeling has been used while all the turbulence features close to the wall are fully resolved (mesh stretching based on hyperbolic tangent function). On the two parallel walls, no-slip boundary conditions are imposed for the streamwise and spanwise velocity. The flow is driven by a constant pressure drop along the channel while periodic boundary conditions are imposed in the two directions of statistical invariance of the flow (streamwise and spanwise). Our aim was to investigate some fundamental aspects of the filtration process assuming that the two parallel permeable walls experience a uniform and steady wall-normal flux. This corresponds to early instants of fouling. As shown in Fig. 1, we impose the cross stream velocity  $u_w$  as a Dirichlet boundary

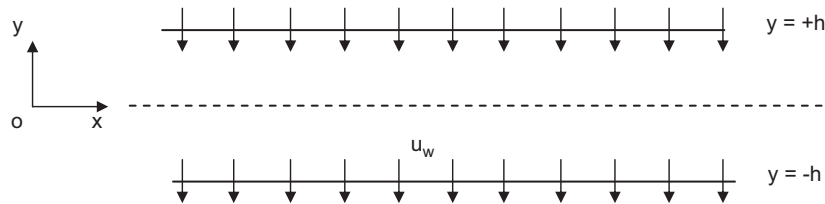


Fig. 1. Sketch of the channel flow considered in the simulations. Arrows correspond to the filtration velocity  $u_w$  normal to the walls.

condition. We simulate the flow in an idealized channel with two parallel permeable walls, with permeation fluxes in opposite directions (outward and inward) to maintain mass balance and keep the mean axial velocity  $\langle \bar{u} \rangle$  constant. This helps to enforce mass conservation through the entire computational domain and permits the use of periodic boundary conditions in the stream-wise direction thus reducing the computational cost of simulation. Of course, in reality the flow is outwards on both walls. Due to low permeability of permeable walls (filtration membrane or porous walls for instance), the pressure difference across the walls is orders of magnitude larger than the pressure drop in the flow direction yielding constant cross-flow flux for short channels. For the analysis of the filtration process, we only dealt with the bottom wall  $y = -h$  where the permeation flux is outward. Although in real cross-flow filtration applications an outward flow should be considered also for the upper permeable wall, the configuration presented in Fig. 1 is valid because the concentration of particles in the bulk is uniform far from walls (see paragraph 4) while strong gradients occur in the vicinity of walls. Therefore, particle transport, adhesion and detachment events occurring on the bottom wall have no correlation with the boundary condition applied on upper wall. Since  $u_w/\langle \bar{u} \rangle \ll 1$ , the turbulent flow structures are not modified by the cross-flow velocity (Hanh et al., 2002).

### 2.1. Validation of a laminar channel flow

We tested the accuracy of the numerical solution under laminar flow conditions ( $Re = 100$ ), with and without the permeation velocity  $u_w$ . An analytic solution of the velocity profile is available in fluid mechanics textbooks (Spurk, 1997) for a plane channel flow as follows:

$$u(y) = \frac{Kh}{\rho u_w} \left( \frac{y}{h} + \frac{e^{u_w h/v} + e^{-(u_w h/v)} - 2e^{(u_w y/v)}}{e^{u_w h/v} - e^{-(u_w h/v)}} \right) \quad (2)$$

where  $u$  is the velocity component parallel to the wall,  $K$  is the opposite of the pressure gradient imposed in the flow direction ( $x$ ). Eq. (2) degenerates towards the well known Poiseuille velocity profile when  $u_w/\langle \bar{u} \rangle \ll 1$ . Comparisons between the velocity profiles calculated with Eq. (2) and the simulation results for different values of the permeation velocity led to relative errors lower than  $10^{-4}$ .

### 2.2. Statistics of the turbulent channel flow

The flow Reynolds number is 4000 based on the average flow velocity and the channel height  $2h$  (this corresponds to 8000 for the classical definition based on equivalent diameter). This is significantly higher than the transition ( $Re_c \sim 2000$ ) preventing the presence of large scale intermittency in our flow configuration. We initiate the velocity field with Eq. (2) and add a certain amount of noise to provoke transition to turbulence. After a transient regime, the flow reaches sustained turbulence with steady statistics. Our simulation domain was chosen large enough to contain the general features of wall-bounded turbulence (streaks, bursts, sweeps and hairpin vortices). However, the longitudinal and spanwise dimensions of the channel were fixed following the study of Xu et al. (2002) (same flow conditions and same mesh). We used a grid composed of  $64 \times 64 \times 64$  nodes equally spaced in two directions  $x$  (flow direction) and  $z$  (spanwise direction). In the  $y$  (wall normal) direction the mesh is stretched near the walls enforcing 4 to 5 nodes in the viscous sublayer. This ensures grid independence of the numerical results especially in the near-wall region (viscous sublayer and buffer layer). The turbulent structures are active in the buffer layer and convected towards the

bulk flow while fluctuations vanish in the viscous sublayer. In those regions of the flow, velocity gradients are steep, which require mesh refinement.

Averages of the velocity field are formed over time and the two directions of homogeneity ( $x, z$ ). All the statistics are very similar to an impermeable turbulent channel flow (see Moin and Kim, 1982) because  $u_w/\langle \bar{u} \rangle$  is extremely low. Based on the profile of the mean velocity, we can define the characteristic friction velocity  $u^* = (\langle \bar{\tau}_w \rangle / \rho)^{1/2}$ , which is related to the mean wall shear stress  $\langle \bar{\tau}_w \rangle$ . The turbulent flow in the vicinity of the wall is characterized by the wall Reynolds number  $Re_\tau = (\langle \bar{\tau}_w \rangle / \rho)^{1/2} h / \nu = 135$ . Therefore, the viscous length  $\delta_v = \nu / (\langle \bar{\tau}_w \rangle / \rho)^{1/2}$  is 135 smaller than the half width of the channel. This gives a measure of the stretching of velocity gradients close to the wall in the turbulent regime. In the remainder of the paper, velocities, lengths and time can be scaled in two ways using either the channel characteristics  $\langle \bar{u} \rangle$ ,  $h$  and  $h/\langle \bar{u} \rangle$  or the wall units (viscous units)  $u^*$ ,  $\delta_v$  and  $\delta_v/u^*$ . When wall units are used, a superscript  $+$  is added otherwise we use the channel units. The spanwise and longitudinal dimensions of the domain correspond to 800 wall units, respectively. This corresponds to the typical length of low speed streaks while six to eight of them can fit in the spanwise width of the domain (Rajaei et al., 1995).

In Fig. 2, the mean velocity profile has been scaled using  $u^+ = \langle \bar{u} \rangle / (\langle \bar{\tau}_w \rangle / \rho)^{1/2}$  and the distance to the wall scaled by  $\delta_v$ . This is a classic presentation of the viscous sublayer  $u^+ = y^+$  for  $y^+ < 5$  and the Log law region for  $y^+ > 50$ . In our simulations, the region of fully developed turbulence is limited because the Reynolds number is moderate. The region (so called buffer layer) located between  $y^+ = 10$  and 30 experiences the most intense velocity fluctuations. In Fig. 3a, the profiles of the three components of the fluctuating velocity scaled by the wall velocity  $u^*$  are shown as a function of  $y/h$ . The maxima are located in the buffer layer between  $y^+ = 10$  and 20. These are in good agreement with the experiments of Kreplin and Eckelman (1979) although  $Re_\tau = 190$  in their experiments. Fig. 3b also shows that the turbulent contribution to the shear stress (the so-called turbulent Reynolds shear stress) grows as the viscous stress decreases away from the wall. All these features have been often commented on in the literature and contribute to the validation of our direct numerical simulations of the flow. More statistics (streaks separation distance, velocity

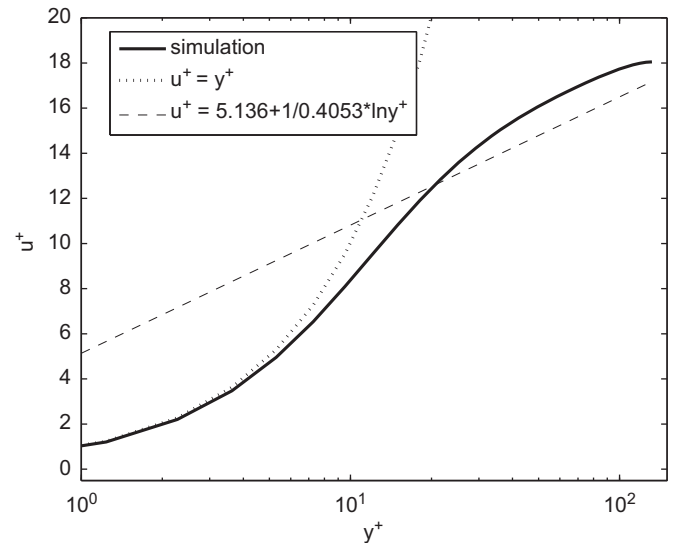
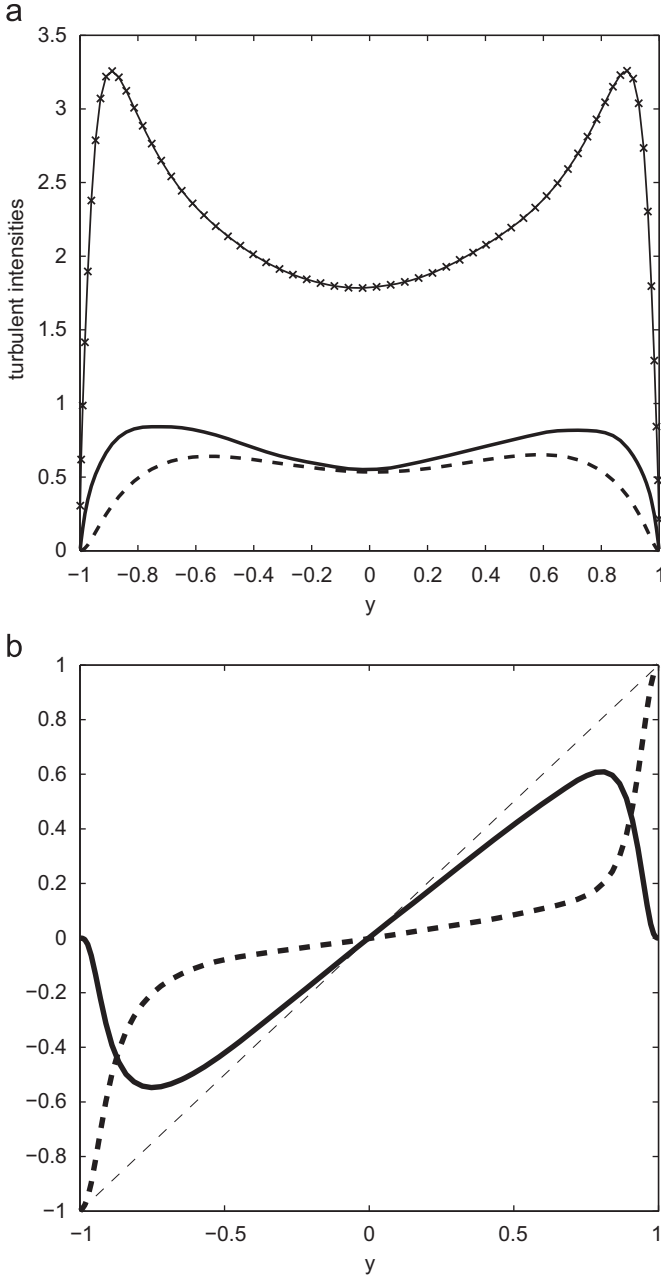


Fig. 2. Dimensionless mean velocity profile vs. distance from the wall (scaled with wall units).



**Fig. 3.** (a) Profiles of the fluctuating velocity scaled by  $u^* = (\langle \tau_w \rangle / \rho)^{1/2}$ . Solid line with x:  $u'$ , dashed line:  $v'$ , solid line:  $w'$ . (b) Total shear stress profile across the channel (thin dashed line). Thick dashed line: viscous contribution  $\mu d\langle u \rangle / dy$ , solid line: Reynolds stress  $-\rho \langle u'v' \rangle$ .

autocorrelations) have been compared to the literature but are not detailed in the present paper.

### 2.3. Near-wall turbulent structures

The dynamics of near-wall turbulence is complex and has been a longstanding topic of research. The complexity arises from the interplay of three major features:

- The no-slip boundary condition on the streamwise component of the velocity damps the fluctuations of the velocity and produces a strong shear normal to the wall.
- The intense shear tends to stretch all the flow structures in the streamwise direction, elongating the fluctuating flow field.

- The presence of the wall forces the redistribution of the turbulent kinetic energy due to the imposed boundary condition on the wall normal velocity. Therefore, in the vicinity of the wall the normal component of the flow velocity tends towards the imposed permeation velocity  $u_w$ .

Because of the strong streamwise stretching, the near-wall turbulence is composed of longitudinal streaks (see Fig. 9a). Those flow structures are elongated in the streamwise direction (typically, the length is a few hundred wall units) and are distributed in the spanwise direction (statistically the distance between two streaks is one hundred wall units). The streaks are flow regions where the fluid is moving slower or faster than the local mean value. They have a limited life time due to a longitudinal instability, which provokes the lift-up of these structures towards the turbulent bulk flow. These turbulent structures (see Fig. 4 for an instantaneous snapshot) are unsteady and contribute to the cycle of regeneration of the turbulence (Jeong et al., 1997). During these events, slow fluid is ejected from the wall region towards the bulk and high-speed fluid is sucked from the bulk and projected towards the wall leading to a local and instantaneous increase of wall shear stress. The transfer of momentum and mass between the wall and the core of the turbulent flow is very intense. The intensity of the fluctuations of the local wall shear stress may be large. Fig. 5 shows the probability density distribution of simulated values of the local wall shear stress fitted by a log-normal law. This has been also observed by Sheng et al. (2009). The unsteady nature of turbulence induces large fluctuations of the local and instantaneous characteristics of the particle dispersion (concentration, fluxes, etc.). Statistics can be formed over space and time. Spatial averages can be easily obtained by summation over the two homogeneous directions ( $x, z$ ) for distinct time steps. Temporal averages have been formed over seven realizations of flow, which reduces fluctuations around the mean value (see Fig. 6).

The low speed and high speed streaks are a central feature of the wall-bounded turbulence and we will see that they have a particular importance on the detachment of particles. Finally, we point out that although the permeation velocity is extremely low and does not influence the general features of the turbulence, it makes a major contribution to particle trajectories in the vicinity of the wall where velocity fluctuations all vanish due to viscous effects. Also, Brownian agitation, which is negligible away from the wall (intense turbulence occurs beyond  $y^+ > 7$ ) is a central feature for particle dispersion close to the wall where turbulence is damped by viscous stresses.

### 3. Lagrangian tracking of particles

To determine the most important features of particle dispersion, we based our analysis on the characteristic dimensionless numbers of the coupling between the particle and the flow length and time scales. We focus on particles with a typical diameter of  $d_p = 1 \mu\text{m}$  and density ratio  $\rho_p / \rho$  equals to 1.5, which is an upper bound for most plastic particles. In our numerical model, we account for particle transport by the flow, Brownian diffusion, adhesion and detachment from the wall.

The time scale of particle dynamics is the viscous relaxation time  $\tau_p = (m_p + m/2) / 6\pi\mu r_p$  with  $m_p, r_p$  being the mass and the radius of the particle and  $m$  the mass of the fluid volume occupied by the particle. It is compared to the fluid flow time scale  $\tau_f = \nu / u^*^2$  through the Stokes number  $\text{St} = \tau_p / \tau_f$ . In the range of physical parameters we investigate,  $\text{St}$  is very small (typically  $\sim 4.5 \times 10^{-4}$ ). The disperse phase behaves as non-inertial particles. Segregation or local accumulation in the flow induced by turbulent near-wall



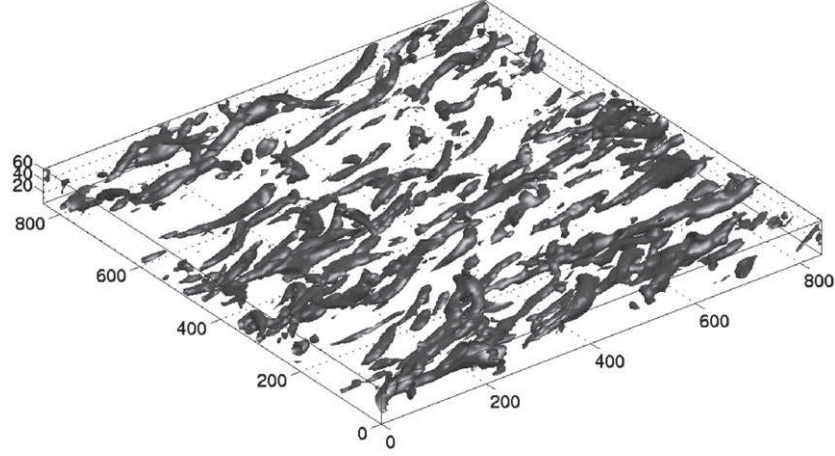


**Fig. 4.** Near-wall turbulent structures located between the bottom wall and  $y^+ = 60$ . The domain dimensions have been scaled with wall units.

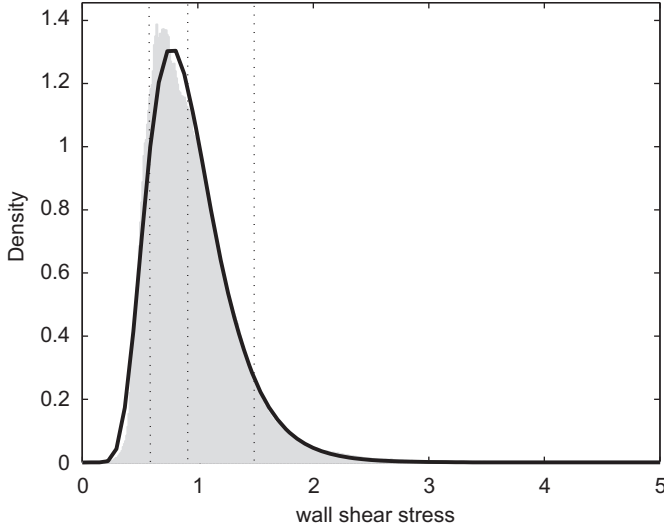


**Fig. 5.** Probability distribution of the wall shear stress scaled by  $\langle \tau_w \rangle$  and its approximation by a lognormal distribution. Vertical dotted lines:  $\tau_{crit}/\langle \tau_w \rangle = 0.57, 0.91, 1.48$ .

structures does not occur (Rouson and Eaton, 2001). It is important to note that the viscous sublayer is significantly thicker than the particle diameter ( $d_p/\delta_v = 0.064$ ). Therefore particles in the vicinity of the wall are fully embedded in the viscous sublayer and will be treated as point particles. Close to the wall ( $y^+ < 1$ ), particles approaching the solid boundary experience an unsteady laminar shear flow (the magnitude is non-uniform over the wall due to the presence of turbulent structures at  $y^+ > 10$ ). Therefore, the effect of Brownian diffusion included in the simulations through a random walk model is important. This can be characterized by the Peclet number of the particles  $Pe = u_w r_p / D_p$  where  $D_p$  is the Stokes–Einstein diffusion coefficient ( $D_p = k_B T / 6\pi\mu r_p$  with  $k_B$  the Boltzmann constant and  $T$  the temperature). Defining the Peclet number with  $u_w$  means that the typical velocity of the particles close to the wall is controlled by the permeation velocity because transverse velocity fluctuations are vanishingly small at the wall. This assumption is valid while the Stokes number is very low and the turbulence intensity is weak in the viscous sublayer. We obtain  $Pe \sim 10$  meaning that Brownian diffusion has a significant contribution to the particle trajectories. Finally, comparing the characteristic velocity of filtration to the settling speed of particles in a quiescent fluid provides an estimation of gravity effects in the

process. Using Stokes drag, we can estimate the settling velocity of the particles under gravity  $\mathbf{g}$ :  $U_{sed} = (m_p - m)g / 6\pi\mu r_p$ . The velocity ratio  $U_{sed}/u_w = 0.05$  clearly shows that the gravitational contribution to deposition is much weaker than the drag induced by the permeation velocity and, thus, gravity will be ignored in our simulations.

### 3.1. Trajectory equation

Using force balance (Eqs. (3) and (4)) acting on an isolated particle, trajectories of individual point particles can be simulated in a Lagrangian framework.

$$\frac{d\mathbf{x}}{dt} = \mathbf{v} \quad \rho_p V \frac{d\mathbf{v}}{dt} = \mathbf{F} \quad (3)$$

The dispersed phase is made of microparticles experiencing the combined effects of the carrying fluid flow and Brownian motion. Obtaining an analytical expression for all hydrodynamic forces is still an open issue in most flow regimes. Therefore, simplifying assumptions have to be adopted to make the problem tractable and obtain a reasonable force balance. Considering that all the relevant spatial length scales of the carrying flow are much larger than the typical size of the particles ( $d_p/\delta_v \ll 1$ ), we assume that the so-called Faxén corrections induced by the local curvature of the flow velocity field are negligible in the expression of all hydrodynamic forces. Also, we considered the particles to be spherical. The particulate Reynolds number is low and Stokes' expression is an appropriate estimation of drag. In addition to the above assumptions, we assume that direct interactions between particles are negligible, which restricts our investigation to dilute suspensions. We write the force balance (Eq. (4)) as a sum of distinct contributions. Hence, we track the particle trajectories and predict the position  $\mathbf{x}(t)$  of their center of mass and their velocity  $\mathbf{v}(t)$  in a fluid flow whose velocity, Lagrangian acceleration, and vorticity at  $\mathbf{x}(t)$  are  $\mathbf{u}$ ,  $D\mathbf{u}/Dt$  and  $\boldsymbol{\omega} = \nabla \times \mathbf{u}$ .

$$\mathbf{F} = -3\pi\mu d_p(\mathbf{v} - \mathbf{u}) + \rho \frac{\pi d_p^3}{6} \frac{D\mathbf{u}}{Dt} + \rho \frac{\pi d_p^3}{6} C_M \left( \frac{D\mathbf{u}}{Dt} - \frac{d\mathbf{v}}{dt} \right) - \rho \frac{\pi d_p^3}{6} C_L(\mathbf{v} - \mathbf{u}) \times \boldsymbol{\omega} \quad (4)$$

In Eq. (4),  $\mathbf{F}$  is the sum of the Stokes drag, dynamic pressure gradient (also called Tchen force), added-mass and lift forces while buoyancy and Basset effects have been neglected. Assuming that particles have a spherical shape  $C_M$  is equal to 1/2 (Magnaudet et al., 1995). For high particulate Reynolds numbers (based on the slip velocity), the mechanisms that control lift effects are essentially of inviscid nature, so that the inviscid result

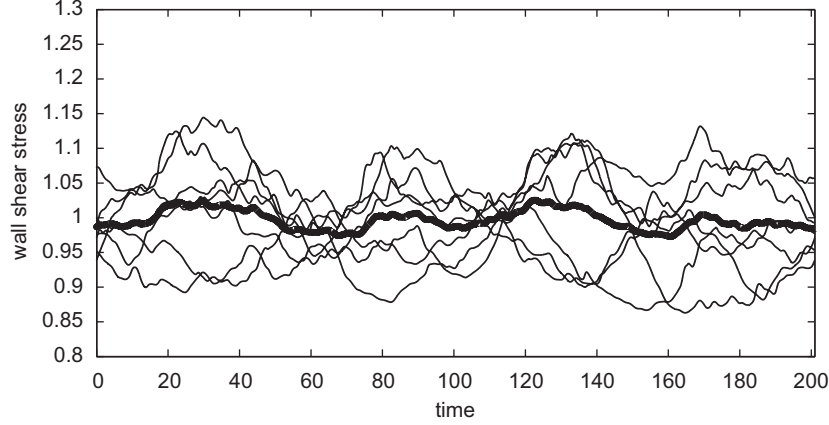


**Fig. 6.** Seven calculations (thin lines) of the mean wall shear stress on the bottom wall and its average (thick line) versus time. Dimensionless time:  $\langle \bar{u} \rangle t/h$ . The wall shear stress is scaled by its overall mean value:  $\langle \tau_w \rangle / \langle \bar{\tau}_w \rangle$ .

$C_L = 1/2$  is appropriate. At lower Reynolds numbers, it was shown that  $C_L$  is a function of both the Reynolds number and the shear rate. In contrast, for Reynolds numbers typically less than unity, the situation becomes much more complex. This is why no general expression of the lift force applicable to an arbitrary linear flow field is available to date in this regime. We used a correlation that matches the Saffmann estimate at low particulate Reynolds number. We did not include wall distance corrections on  $C_M$  and  $C_L$  as the particles approach the wall. In the viscous sublayer, the contribution of Brownian motion is largely dominating the particle dynamics.

This system of ordinary differential equations can be efficiently solved with a four-step forward Runge–Kutta scheme. All the information about the fluid quantities (velocity and its gradients) is interpolated by a tri-linear scheme at the particle position. In the viscous sublayer, the components of the velocity vary smoothly and using a higher order scheme is not necessary. Brownian motion is accounted for by a random walk (Eq. (5)) supplemented to the deterministic particle position obtained from Eqs. (3) and (4). The stochastic contribution is added explicitly at the end of each time step of the deterministic particle integration  $\Delta \mathbf{x}^{\text{det}}$ .  $\xi_i(t)$  is a random number based on a Gaussian probability density function with zero mean and standard deviation equal to one.

$$\Delta \mathbf{x}_i = \Delta \mathbf{x}_i^{\text{det}} + \xi_i(t) \sqrt{2D_p \Delta t} \quad (5)$$

The numerical solution of the set of stochastic equations was validated under simplified conditions. The dispersion of an initially homogeneous particle suspension was simulated considering a constant wall normal velocity  $u_w$ . For this test, the condition of perfect particle rebound on the wall was imposed. Under steady state, the particle concentration profile is known analytically (balancing convection and diffusion fluxes gives an exponential decrease of the concentration profile). We obtained an excellent agreement between the analytical prediction and the simulation results (relative error lower than  $10^{-2}$ ).

### 3.2. Behavior in the vicinity of the wall

Because we are interested in the simulation of Brownian motion of particles very close to the wall, we have to precisely resolve the stochastic contribution in the vicinity of the wall. This is a major feature for accurately predicting the adhesion flux.

When a stochastic differential equation corresponding to the Lagrangian tracking of the particles is solved in the vicinity of an

absorbing boundary (i.e. deposition wall), the limitation of using a finite time step  $\Delta t$  has been addressed by the “optimal stopping” technique (Mannella, 1999; Maniero and Canu, 2006). During a single time step, a selected particle may have reached the wall even though the initial and the final positions remain on the same side of the boundary representing the wall. A simulation in similar conditions but with a much shorter time step would have correctly predicted this adhesion event. Therefore, the probability of particle deposition during each time step has to be evaluated for complementing the numerical prediction. This estimate is based on the probability  $P(\text{hit})$  as follows:

$$P(\text{hit}) = \exp \left[ - \frac{(y_w - y_0)(y_w - y_s)}{D_p \Delta t} \right] \quad (6)$$

The subscripts  $w$ ,  $0$  and  $s$  indicate the wall location, and the initial and final positions for the considered time step, respectively.  $P(\text{hit})$  is calculated at each step for each particle. This predicts whether the particle crosses the wall boundary and therefore determines the precise deposition time and location. Alternative schemes such as reduction of the time step or variable time step methods are much more time consuming (Kloeden and Platen, 1992). In Eq. (6) the double-layer electric repulsion is ignored but this physical–chemical effect may be accounted for by modifying  $P(\text{hit})$  (see Mannella, 1999). Only the attractive Van der Waals force is accounted for with a perfect sink model. In order to determine colloidal motion near the wall, an explicit Van der Waals force can be considered in the force balance (Eq. (4)). A correct description of the Van der Waals interaction should include retardation and screening effects (Russel et al., 1989; Maniero and Canu, 2006), which limit its range of influence to a few nanometers. In many engineering applications, the non-retarded and non-screened expression of the Van der Waals force is applied, leading to an overestimation of its interaction length as discussed by Israelachvili (1991) and Maniero and Canu (2006). The deposition rate due to this very short range attraction force is appreciably smaller than that of the hydrodynamic forces considered in Eq. (4) (Maniero and Canu, 2007). Therefore, using Eq. (6) introduces negligible errors (Maniero and Canu, 2007). In the force balance (Eq. (4)), we did not include deterministic particle wall interactions such as electric double layer repulsion. This physical–chemical effect is undoubtedly very important in the real process but as a first step of our numerical modeling we chose conditions that allow some simplifications. We consider negligible electrical double layer repulsion therefore only Van der Waals particle–wall interaction is present (see the model of adhesion in next section). Similar conditions can be achieved

with aqueous suspensions of well-defined ionic strength, tunable through the pH value, keeping the interacting surfaces near the isoelectric point. Since only the attractive Van der Waals interaction acts on non-inertial particles, we assume that the efficiency of adhesion onto the wall is maximum and equals one. Consequently, when particles reach the wall they attach (perfect sink model).

The efficiency of the optimal stopping technique can be emphasized through the simulation of a simplified problem (Maniero and Canu, 2006). In a uniform flow, the particle motion in the wall normal direction is only controlled by Brownian diffusion and convective transport towards the absorbing wall. In his reference textbook, Fuchs (1964) gave an explicit expression relating the diffusion coefficient  $D_p$  to the probability distribution of particle impact times on the wall. We carried out four distinct simulations comparing the effect of the optimal stopping technique for two different initial positions away from the wall. This test clearly shows that using the optimal stopping technique significantly increases the accuracy of the simulations, especially when the particles are initially positioned in the vicinity of the wall. The error is decreased by a factor 20 for an initial position of  $y^+ = 0.0135$ . The role of the optimal stopping technique increases as the particle/wall initial distance decreases. Our study involves particles experiencing detachment from the wall, entrainment in the flow and possibly adhesion again. There will be a large number of trajectories confined in a narrow region very close to the wall and adhesion fluxes may be greatly underestimated without the optimal stopping technique.

### 3.3. Modeling the detachment

Particle detachment from a surface under laminar or turbulent conditions has been investigated in several works. Yiantsios and Karabelas (1995) studied the adhesion and detachment of spherical glass particles from a flat glass surface both theoretically and experimentally. Their results suggested that the rolling mechanism is mainly the cause of detachment in their range of parameters. Ziskind et al. (1995, 1997) presented an exhaustive review and analysis of different approaches related to particle re-entrainment in turbulence.

Three mechanisms of detachment are commonly considered: lifting, sliding and rolling (Burdick et al., 2001). A complete description of particle detachment should simultaneously consider all three of these mechanisms. However, under the physical configuration and the range of parameters we considered (particles are completely embedded within the viscous sublayer where the velocity fluctuations normal to the wall are very weak), it is possible to ignore the lifting mechanism due to forces acting perpendicularly to the wall. Moreover, recent investigations on particle detachment in similar conditions, suggest that the rolling mechanism prevails over sliding (Yiantsios and Karabelas, 1995). Consequently, we consider only the rolling mechanism to determine the criterion for detachment (see Fig. 7). After detachment, the trajectory including all the contributions, is integrated and due mainly to the Brownian diffusion particles moving away from the wall. The rolling criterion is given in the following equation as a torque balance where  $M_D$  is the hydrodynamic torque induced by surface stresses,  $F_D$  the drag force parallel to the wall,  $l_1$  the distance from the particle center to the wall,  $F_L$  the lift force (which makes a negligible contribution),  $l_2$  the radius of contact area and  $F_A$  the adhesion force:

$$\overline{M_D} + \overline{F_D l_1} + \overline{F_L l_2} \geq \overline{F_A l_2} \quad (7)$$

Considering Eq. (7) as the detachment condition yields detachment when the torque related to external forces overcomes the torque of adhesion forces. In Eq. (8), the total torque acting on an

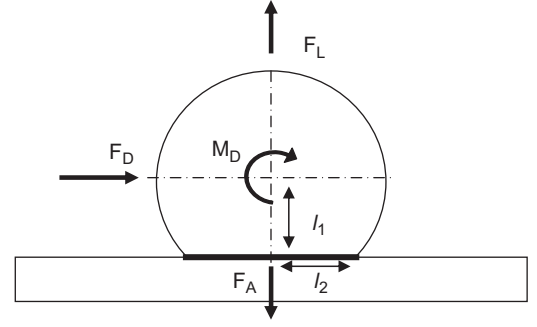


Fig. 7. Sketch of a particle attached to a flat wall.

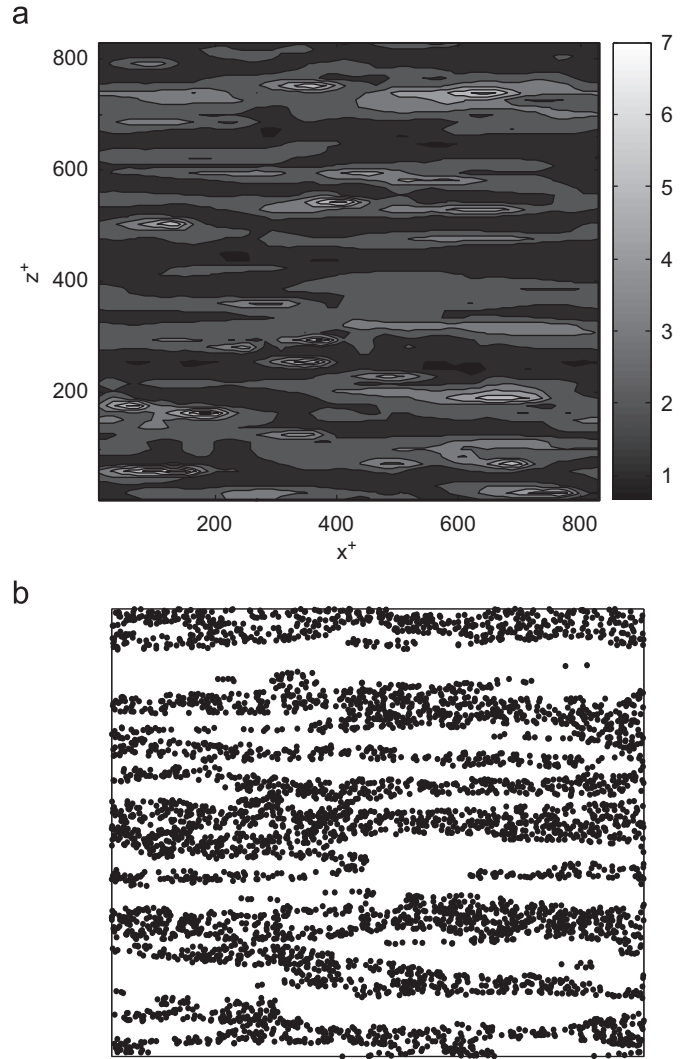


Fig. 8. (a) Snapshot of the spatial distribution of the wall shear stress  $\tau_w$  scaled by  $\langle \tau_w \rangle$ . (b) Instantaneous snapshot of particles attached onto the wall ( $\tau_{crit} / \langle \tau_w \rangle = 0.91$ ,  $s_{clean} = 50\%$ ).

attached particle is expressed in terms of local shear rate (Ziskind et al., 1995, 1997; Yiantsios and Karabelas, 1995).

$$\overline{M_T} = \overline{M_D} + \overline{F_D l_1} = 44 \tau_w r_p^3 \quad (8)$$

When a particle is attached to a flat wall, deformations from its original spherical shape occur and consequently the contact area may change. Calculating the right hand side of Eq. (7) needs



**Table 1**  
Dimensionless flux of attachment for different critical wall shear stresses of particle detachment.

	$\tau_{crit}/\langle \bar{\tau}_w \rangle = \infty$ ; $s_{clean}=0$ absorbing wall (pure adhesion)			$\tau_{crit}/\langle \bar{\tau}_w \rangle = 1.49$ $s_{clean}=0.2$	$\tau_{crit}/\langle \bar{\tau}_w \rangle = 0.91$ $s_{clean}=0.5$	$\tau_{crit}/\langle \bar{\tau}_w \rangle = 0.57$ $s_{clean}=0.9$
	Simulation results	Minnikanti et al. (1999)	Song and Elimelech (1995) model adapted to turbulent conditions	Simulation results	Simulation results	Simulation results
Sh from Eqs. (12) or (17)	$1.6 \times 10^5$	$1.23 \times 10^5$	$1.84 \times 10^5$	$1.2 \times 10^5$	$0.48 \times 10^5$	$0.34 \times 10^5$

evaluation of the deformation of attached particles. Particle deformation depends on the mechanical characteristics of the wall, the particle nature and the energy of adhesion. We consider the Johnson–Kendall–Roberts model (1971), commented in the textbook of Israelachvili (1991), to predict particle deformation (Ziskind et al., 1997). The torque of adhesion (right hand side of Eq. (7)) is approximated in Eq. (9) where  $\omega_A$  is the work of the adhesion force and  $K_e$  the reduced elastic modulus. These two physical quantities depend on the properties of the particle and the particle/wall interaction.

$$\overline{M_A} = 2.63 \frac{\omega_A^{4/3} d_p^{5/3}}{K_e^{1/3}} \quad (9)$$

Rearranging Eqs. (7)–(9), the value of  $\tau_{crit}$  can be estimated based on the physical (reduced elastic modulus  $K_e$ ) and physical–chemical (work of the adhesion,  $\omega_A$ ) nature of particles and wall (Eq. (10)).

$$\tau_{crit} = \frac{\overline{M_A}}{44r_p^3} \quad (10)$$

In the present work, we varied the value of the critical wall shear stress between 2.6 and 6.75 Pa; these values remain within the range of experimentally determined critical shear stress. In the literature, several experiments have reported values of the yield stress for particle detachment within the range 2–20 Pa (Negri et al., 2002) depending on the nature of the particles (shape, material) and the duration of contact (Yiantsios and Karabelas, 1995).

It is straightforward to use Eq. (10) with the direct numerical simulation of the flow. The simulations provide an instantaneous and spatial distribution of the wall shear stress  $\tau_w(x, -h, z, t)$  (see Fig. 8a) under turbulent conditions. Hence Eq. (10) gives the criterion for detachment  $\tau_w > \tau_{crit}$  for an attached particle at any location. The critical wall shear stress has to be compared to the probability distribution of simulated values (Fig. 5). Depending on the critical wall shear stress for detachment determined by Eq. (10), the cumulative probability distribution can be used to estimate the average wall area, which matches the detachment condition. This particular fraction  $s_{clean}$  of the wall area is called “clean surface” in the remainder of the paper because particles initially attached to this wall area are instantaneously resuspended in the fluid flow. It is defined by  $s_{clean} = (S_{clean}/S)$  where  $S_{clean}$  is the area of the surface matching  $\tau_w > \tau_{crit}$  and  $S$  the total surface of the permeable bottom wall. For perfectly absorbing walls  $s_{clean}$  equals zero (no detachment associated to permanent adhesion) while for a perfect rebound condition  $s_{clean}$  equals unity. The correspondence between  $\tau_{crit}/\langle \bar{\tau}_w \rangle$  and  $s_{clean}$  is collected in Table 1.

#### 4. Discussion of results

Simulations including the full set of models simultaneously, i.e. particle transport by the turbulent flow and Brownian motion,

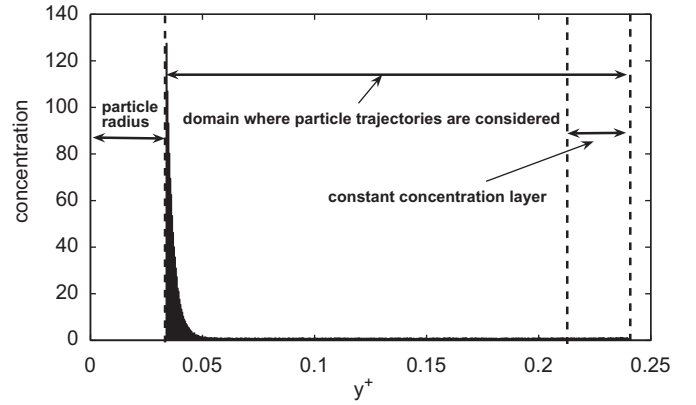


**Fig. 9.** The particle boundary layer (concentration scaled by  $c_{bulk}$ ). Example of concentration profile obtained in the simulations for  $s_{clean}=90\%$ .

adhesion onto the permeable wall, detachment and possibly re-entrainment or re-deposition were carried out. To obtain converged statistics, a large number of particles have to be considered. We focused on wall normal concentration profiles, temporal evolution of the number of attached particles, deposition and resuspension fluxes. A complete set of data is based on averaging over seven simulations (initial transients are not considered in the statistics). The simulation starts with a total of 20,000 particles; 10,000 particles randomly dispersed throughout the domain where the particle trajectory is considered (see Fig. 9) and 10,000 particles attached to the wall. The presence of the attached particles reduces the transient time of the particulate boundary layer formation. We expect this mass boundary layer to be much thinner than the hydrodynamic viscous sublayer. For Brownian dispersions embedded in a turbulent channel flow and experiencing irreversible deposition, the thickness of the mass boundary layer  $\delta_c$  is related to the hydrodynamic length  $\delta_v$  and the Schmidt number  $Sc = \mu/\rho D_p$  (Calmet and Magnaudet, 1997) by Eq. (11).

$$\delta_c \approx Sc^{-(1/3)} \delta_v \quad (11)$$

Applying Eq. (11) to our physical parameters leads to  $\delta_c^+ = 0.0358$  wall units. This approximate value of the boundary layer thickness is based on conditions of irreversible adhesion without filtration flux. An even thinner concentration boundary layer is expected when the filtration flux is present. In our numerical model, we need to simultaneously solve the flow field by Direct Numerical Simulation and obtain all the particle trajectories. Although we are interested in phenomena taking place in the near-wall region, we need to simulate the flow dynamics in the bulk because the buffer layer and the region of developed turbulence influence the local and instantaneous distribution of wall shear stress and the flow profile in the viscous sublayer. To reduce the computational cost of the simulations, instead of distributing the particles evenly throughout the entire domain, we restricted the simulation of the trajectories to a region very close to the wall ( $y^+ < 0.227$ ). Indeed, we are concerned with non-inertial particles, which are likely to be homogeneously

distributed in the bulk (very low Stokes number). Consequently, concentration gradients are present only in a thin concentration boundary layer near the wall. We impose a “constant concentration layer” sufficiently far from the wall (see Fig. 9); note that the “constant concentration layer” is located at a distance rather larger than the value of  $\delta_c^+$  evaluated from Eq. (11). During the simulations, the number of particles located between  $y^+ = 2.11 \times 10^{-1}$  and  $y^+ = 2.27 \times 10^{-1}$  are frequently counted and new particles are added or removed in this region to keep the number density of particles constant and equal to its reference value. The practice to “add and remove” particles in this region is very efficient. The constant bulk concentration imposed far from the mass boundary layer only fluctuates within 1% over time. Based on the instantaneous positions of the particles, concentration profile is formed by box counting. Slabs parallel to the wall are used to calculate the number of particles associated to a particular wall normal distance. The thickness of these slabs is fine enough to resolve steep concentration gradients in the boundary layer and wide enough to contain many particles for statistical convergence. The thickness  $\Delta y^+$  has been set to  $2.27 \times 10^{-4}$ . The quantitative value of the bulk volumetric concentration in our simulations is only considered as a reference while we used it to scale the concentration profiles. Because we ignore direct particle-particle interaction and the modification of the flow by the presence of particles, the range of applications in terms of mass loading of particles is limited to very dilute suspensions.

The build-up of the concentration layer is basically time dependent because the layer of constant concentration away from the wall acts as a continuous source of particles transported towards the wall by the permeation velocity. Consequently the total number of particles involved in the simulations starts at 20,000 and increases continuously during the simulation. The procedure described above was repeated for three different values of the critical wall shear stress: 6.75, 4.16 and 2.6 Pa ( $\tau_{crit}/\langle \tau_w \rangle = 1.48; 0.91; 0.57$ , respectively) corresponding to  $s_{clean}$  equal to 20%, 50% and 90%, respectively (average fraction of the wall area matching the detachment criterion  $\tau_w > \tau_{crit}$ ). Also, the two limiting conditions of irreversible adhesion and particle rebound at the wall have been simulated as references under extreme conditions.

#### 4.1. Local analysis of adhesion

Since the presence of filtration velocity towards the wall induces a source of particles ( $u_w c_{bulk}$ ), the number of particles increases in the near wall region, resulting in a progressive build up of the concentration boundary layer and fouling. Moreover, under turbulent flow conditions the local distribution of attached particles is not likely to be uniform because of the presence of near-wall coherent flow structures yielding spatial fluctuations of the convective flux towards the wall and strong inhomogeneities of wall shear stress leading to particle detachment. As expected, preferential adhesion and re-entrainment locations are spatially correlated to low shear stress areas (see Fig. 8a–b). This is a visual observation of the basis of several theoretical models: local flow structures are responsible for particle detachment and re-entrainment (Ziskind et al., 1995). Using direct numerical simulation of a planar turbulent channel flow (without wall normal velocity), Zhang and Ahmadi (2000) showed that these preferential locations of re-suspension may exist and depend on the nature of the particle (size, adhesion force). We confirm the early observation of Yung et al. (1989) on the interaction between turbulent burst activity and deposited particles. Particles experiencing a wall shear stress lower than the threshold  $\tau_{crit}$  (Eq. (10)) remain attached. The region where  $\tau_w > \tau_{crit}$  corresponds to rapid flows sweeping the wall and is distinct from fluid ejection or bursting.

Particles fully embedded in the viscous sublayer are not lifted up by fluid ejection but initially roll along the wall (Ziskind et al., 1995), are dispersed by Brownian agitation and are eventually dragged towards the bulk by the flow bursting out of the viscous sublayer. There are only few experiments, which quantify the local deposit of small particles on membranes under turbulent flow. One of these techniques is Direct Observation Through Membranes (DOTM), which allows the visualization of the surface of a membrane during filtration. However, these experiments have only been performed for a Reynolds number of 2000 (Li et al., 2003). These experiments revealed the formation of cylindrical rolling flocs during the detachment of bacteria from the membrane surface. However, this technique does not allow the percentage of the fouled surface or its correlation with local shear stress to be determined. There is then no quantitative comparison possible with our work and we could hypothesize that this phenomenon (of cylindrical rolling aggregate) is related to the dynamics of wall-bounded turbulent flows.

The filtration velocity, together with re-suspension, yields particle accumulation close to the wall where the maximum concentration is reached. Fig. 10 plots the maximum concentration scaled by the bulk concentration for different values of the critical wall shear stress versus time. A large fraction of wall area matching the detachment criterion corresponds to larger maximum concentration in the particulate boundary layer. Also the rate of build-up (the slope of linear fitting of simulation results) of the boundary layer is faster. Additionally, the number of particles attached onto the wall (Fig. 11) increases with time. This is a direct measure of the dynamic fouling of the permeable wall. Smaller values of  $\tau_{crit}/\langle \tau_w \rangle$  lead to fewer attached particles. However, we obtain an increase in the number of attached particles although particles can detach easily from the wall. Slow fouling occurs whatever the configuration. It can be explained by the continuous build-up of the particulate boundary layer induced by the filtering flux towards the wall.

#### 4.2. Comparison to macroscopic models

The particulate flux of attachment  $\Phi_{attach}$  is commonly scaled to form the Sherwood number (Eq. (12)). In Fig. 12, the particulate flux obtained in simulations under the configuration of irreversible adhesion ( $s_{clean}=0$ ;  $\tau_{crit}/\langle \tau_w \rangle = \infty$ ) is compared to the

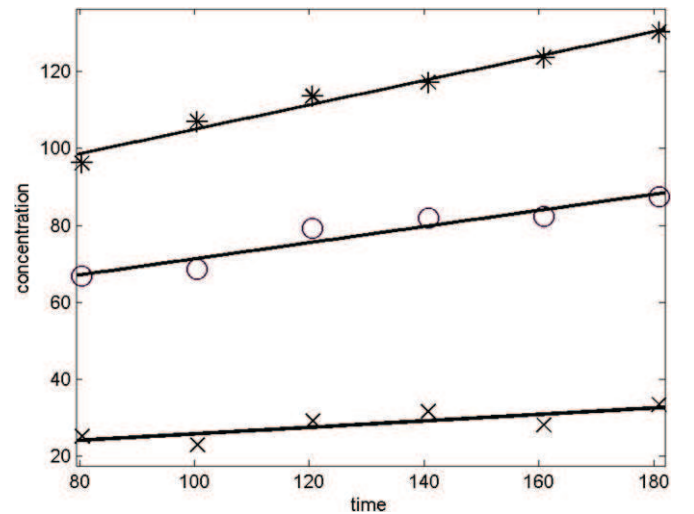
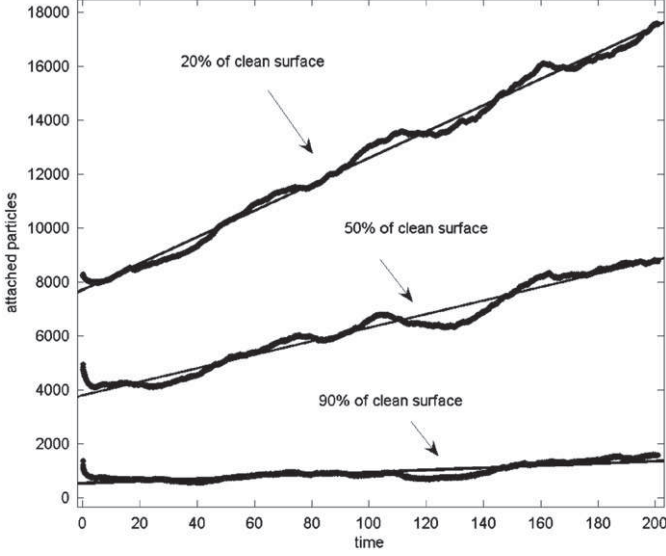
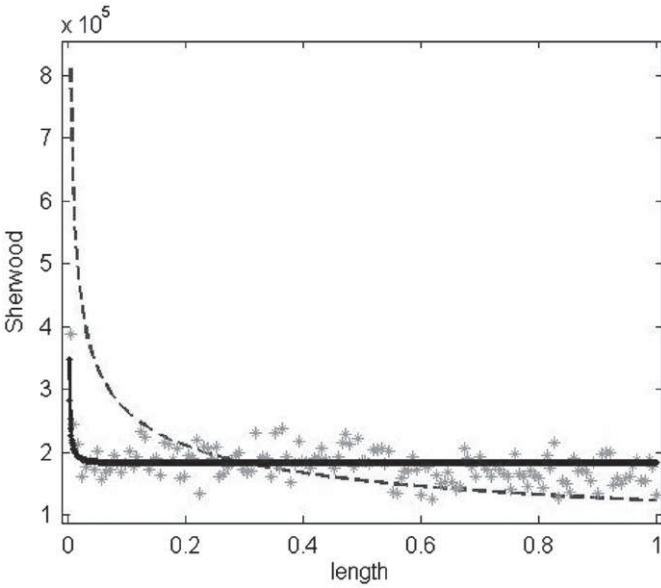


Fig. 10. Maximum concentration scaled by the bulk concentration versus time. Symbols stand for the simulation results averaged in space and over seven simulations (the line is a linear fit). Stars:  $s_{clean}=90\%$ ; circles:  $s_{clean}=50\%$ ; crosses:  $s_{clean}=20\%$  ( $\tau_{crit}/\langle \tau_w \rangle = 0.57, 0.91, 1.48$ , respectively). Dimensionless time =  $\langle \bar{u} \rangle t/h$ .



**Fig. 11.** Number of attached particles versus time (“clean surface” denotes the average fraction of the total wall surface matching Eq. (10)). The thin line corresponds to a linear fit. Dimensionless time:  $\langle \bar{u} \rangle t/h$ .



**Fig. 12.** Streamwise profile of the Sherwood number. Stars: simulation results at different times ( $s_{\text{clean}}=0$ ,  $\tau_{\text{crit}}/\langle \bar{\tau}_w \rangle = \infty$ ); dashed line: Minnikanti et al. (1999); solid line: Song and Elimelech (1995) model designed for turbulent conditions. Dimensionless length:  $\langle \bar{u} \rangle t/h$ .

theoretical models of Song and Elimelech (1995) and Minnikanti et al. (1999). Due to periodic boundary conditions, the temporal evolution of our simulation can be analyzed in terms of normalized spatial evolution using the relation  $\langle \bar{u} \rangle t/h$ .

$$Sh = \frac{h\Phi_{\text{attach}}}{D_p c_{\text{bulk}}} \quad (12)$$

Minnikanti et al. (1999) based their analysis on the solution of a convective diffusion equation (Eq. (13)) of particle transport within the viscous sublayer. Including the effect of wall suction  $u_w$ , they assume a linear profile of the longitudinal velocity. The shear intensity  $k$  is controlled by the average value of shear stress

at the wall under turbulent regime (Eq. (14)).

$$ky \frac{\partial c}{\partial x} - u_w \frac{\partial c}{\partial y} = D_p \frac{\partial^2 c}{\partial y^2} \quad (13)$$

$$u = \frac{0.0395 \langle u \rangle^2}{\nu} \text{Re}^{-(1/4)} y = ky \quad (14)$$

Imposing  $u_w x^{1/3}$  constant along the channel, Minnikanti et al. (1999) obtained a self-similar analytic solution of Eq. (13). A significant discrepancy between our simulation results and the prediction of Minnikanti’s model is observed (Fig. 12) at the channel inlet. The discrepancy is basically related to the assumption of constant  $u_w x^{1/3}$  in theoretical modeling while in our simulations the filtration velocity has been kept constant along the channel length. The different assumptions on the filtration velocity evolution used in our simulation ( $u_w$  is constant) and in Minnikanti’s model ( $u_w \sim x^{-1/3}$ ) can be justified. In both cases the dispersed phase has a non-inertial behavior. Although our particles behave as Brownian particles (typical dimension around one micron) our results can not be extended to flowing suspension of smaller particles. Minnikanti’s model (1999) is suitable for a suspension consisting of small particles (typically macromolecules) and larger concentration is considered. The wall accumulation forms a gel-like concentration polarization layer following the classical  $x^{1/3}$  evolution of the transfer coefficient for a non-slip boundary. In response to this accumulation the filtration velocity decreases along the wall ( $u_w \sim x^{-1/3}$ ). In our case, we are modeling and simulating early instants of deposition of a highly dilute dispersion of Brownian particles and constant filtration velocity  $u_w$  is consistent with other assumptions such as one-way coupling (the particles are not perturbing the flow neither in the bulk nor for the wall boundary condition on filtration velocity).

The model of Song and Elimelech (1995), considered a constant permeation velocity. However, their model was initially developed for laminar flows. Song and Elimelech included in their transport equation the contributions of gravitational, lift and Van der Waals forces. Neglecting the lift and Van der Waals forces terms and considering the mean shear rate in the viscous sublayer of a turbulent channel flow (Eq. (14) similarly to Minnikanti’s model), Eq. (13) can be solved numerically. For a constant filtration velocity  $u_w$  along the channel length, the numerical integration of Eq. (13) is carried out with the following boundary conditions: constant concentration at the inlet of the channel  $c(0,y)=c_{\text{bulk}}$ , “perfect sink model” at the wall  $c(x,0)=0$  and fixed bulk concentration  $c(x,\infty)=c_{\text{bulk}}$  outside the concentration sublayer. These boundary conditions have been also selected by Song and Elimelech (1995) and they are in perfect agreement with our simulation assumptions (particles are assumed to be attached when they touch the wall, i.e. “perfect sink model”; on the contrary in Minnikanti’s model a Robin-Mixed boundary conditions is applied at the wall, where the permeation flux is accounted for, while it is not present in our study. For these appropriate conditions, a good agreement between the numerical solution of Eq. (13) and our Eulerian–Lagrangian simulations are observed in Fig. 12. The comparison to the Elimelech and Song model has been done simply by introducing the mean shear rate provided by DNS in the viscous sublayer, in order to adapt their model (originally developed for laminar flow) to turbulent conditions. Therefore the excellent agreement obtained signifies that while turbulent fluctuations have an important effect on the mechanism of detachment, they are a negligible contribution to particle transport (turbulent diffusion is much larger than Brownian diffusion far from the wall) and attachment onto the wall. Predictions based on mean flow characteristics are sufficient to provide an accurate description of these latter phenomena.

#### 4.3. Determination of particle fluxes

In our simulations, we have direct information on the respective contributions to the balance of particulate fluxes. The rate of increase in the number of suspended particles (Eq. (15)) is the sum of the convective flux entering the simulation domain through the constant concentration layer (far from the wall), the diffusive flux of adhesion and the detachment flux from the wall. A similar balance can be written for the attached particles (Eq. (16)). The rate of increase of total number of particles  $N_{tot} = N_{susp} + N_{att}$  in the simulation domain is equal to  $u_w c_{bulk}$ .

$$\frac{dN_{susp}}{dt} = \left[ u_w c_{bulk} - D \frac{\partial c}{\partial y} \right]_{wall} S + \Phi_{detach} S \quad (15)$$

$$\frac{dN_{att}}{dt} = \left[ D \frac{\partial c}{\partial y} \right]_{wall} S - \Phi_{detach} S \quad (16)$$

Each term of Eqs. (15) and (16) has been calculated in the simulations with  $s_{clean} = 20\%$ ,  $50\%$  and  $90\%$ . Nevertheless, the instantaneous quantities are very noisy due to the unsteadiness of the turbulence. When averaged over the seven flow calculations, the quasi-linear variation of all fluxes in time is related to the continuous and constant feed of the mass boundary layer by the outer boundary condition  $c = c_{bulk}$ . Fig. 10 gives an indication of the continuous build-up of the particulate boundary layer. A linear increase in time of the number of attached particles  $N_{att}$  with distinct slopes is obtained for the three ratios  $\tau_{crit}/\langle \bar{\tau}_w \rangle$  (Fig. 11). The resulting adhesion flux can be scaled to compare our numerical results with the former theoretical predictions of Minnikanti et al. (1999) or Song and Elimelech (1995) modified for turbulent conditions. For  $s_{clean} = 0$  ( $\tau_{crit} = \infty$ ), the Sherwood number (Eq. (12)) compares the flux of adhesion to the diffusion transport of particles. The theoretical estimate is in good agreement with dynamic simulations under turbulent conditions (see Table 1 and Fig. 12). This corresponds to the perfect sink model. For  $s_{clean} \neq 0$  (finite value of  $\tau_{crit}$ ), we propose to extend the definition of the Sherwood number (Eq. (17)) to the simultaneous presence of adhesion and detachment of particles at the wall. The effective adhesion flux corresponds to the net attachment flux:  $\Phi_{eff} = \Phi_{attach} - \Phi_{detach} = dN_{att}/dt$ .

$$Sh = \frac{h \Phi_{eff}}{D_p c_{bulk}} \quad (17)$$

The results of our simulations are summarized in Table 1. It is clear that reducing the critical wall shear stress of detachment yields a reduction of the net attachment flux  $\Phi_{eff}$  since particles increasingly undergo re-suspension in the flow (see Fig. 13 for a comparison of detachment fluxes and their linear fitting). Decreasing the ratio  $\tau_{crit}/\langle \bar{\tau}_w \rangle$  corresponds not only to larger values of the detachment flux but also its rate of increase and consequently larger values of the maximum concentration in the boundary layer (see Fig. 10).

#### 4.4. Temporal evolution of adhesion

The particle fluxes towards ( $\Delta N_{att}/t$ ) or away from the wall ( $\Delta N_{susp}/t$ ) can be scaled by the rate of particles entering the concentration boundary layer (Eqs. (18) and (19)):

$$n_{susp} = \frac{\Delta N_{susp}}{\Delta N_{tot}} = \frac{N_{susp}(t) - N_{susp}(t=0)}{S u_w c_{bulk} t} \quad (18)$$

and

$$n_{att} = \frac{\Delta N_{att}}{\Delta N_{tot}} = \frac{N_{att}(t) - N_{att}(t=0)}{S u_w c_{bulk} t} \quad (19)$$

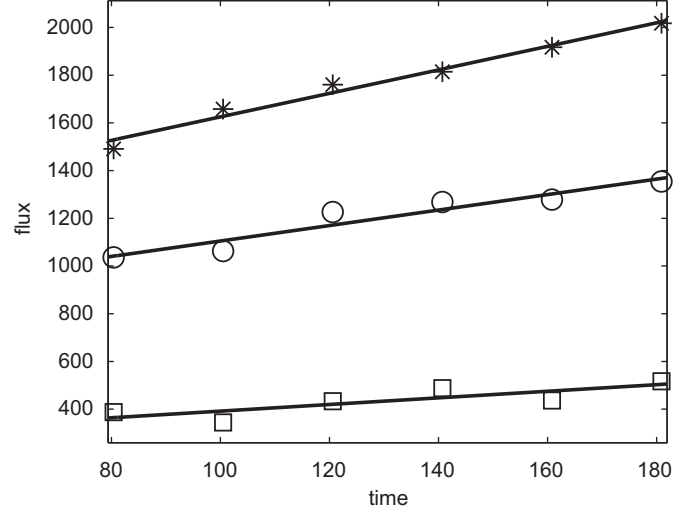


Fig. 13. Detachment flux versus time for three configurations:  $s_{clean} = 90\%$  (stars),  $50\%$  (circles),  $20\%$  (squares) ( $\tau_{crit}/\langle \bar{\tau}_w \rangle = 0.57; 0.91; 1.48$ , respectively). Symbols stand for the simulation results averaged in space and time. Flux densities are scaled by  $u_w c_{bulk}$ . Dimensionless time:  $\langle \bar{u} \rangle t/h$ .

where  $N_{susp}$  is the total number of suspended particles,  $N_{att}$  the total number of attached particles,  $N_{tot}$  the total number of particles and  $S$  the area of the bottom wall. The dimensionless flux of attached particles (or suspended particles) is an indicator of the dynamic fouling of the permeable wall.

Under the condition of absorbing wall ( $s_{clean} = 0$ ,  $\tau_{crit} = \infty$  no detachment)  $n_{susp}$  tends to zero while with perfect rebound ( $s_{clean} = 1$ ,  $\tau_{crit} = 0$ )  $n_{susp}$  tends towards 1. For finite values of  $\tau_{crit}$ , the prediction of  $n_{susp}$  (or  $n_{att} = 1 - n_{susp}$ ) is not obvious. Assuming a perfectly homogeneous suspension from the bulk to the wall (absence of a mass boundary layer), Eq. (18) becomes:

$$n_{susp} = \frac{u_w c_{bulk} t s_{clean}}{u_w c_{bulk} t S} = s_{clean} \quad (20)$$

While formation of a concentration boundary layer close to the wall increases the convective and diffusive fluxes towards the wall, and therefore  $n_{susp} < s_{clean}$  is expected, dynamic re-suspension due to moving near-wall turbulent structures increases the number of suspended particles (increasing  $n_{susp}$ ) compared to its static estimate (Eq. (20)). Fig. 8a is a static snapshot of the wall shear stress spatial distribution. Turbulent streaks and consequently high wall shear stress areas move in time in a streamwise direction. Attached particles in front of the translating region of high wall shear stress will be re-suspended away from the wall while Eq. (10) is verified. Because these two physical mechanisms make opposite contributions, the actual value of the dimensionless flux of particles away from the wall  $n_{susp}$  depends on the relative magnitudes of the two terms. Based on simulation results, we calculated the suspension response for three different conditions of the detachment criterion  $\tau_{crit}/\langle \bar{\tau}_w \rangle = 1.48, 0.91$  and  $0.57$  ( $s_{clean} = 20\%$ ,  $50\%$  and  $90\%$ , respectively). They are plotted against time in Fig. 14. In all cases, the results are close to the static estimate (Eq. (20)). When  $s_{clean} = 20\%$ , the magnitude of  $n_{susp}$  is slightly lower than  $s_{clean}$ . This means that enhancement of the diffusive flux towards the wall dominant over the dynamic detachment effect. The wall area swept by moving regions of high shear stress yields a lower flux away from the wall than the deposition flux. The opposite trend is observed when  $s_{clean} = 50\%$  or  $90\%$ . The explanation is related to the spanwise extension of the wall area matching Eq. (10) for detachment. As  $s_{clean}$  increases, the dynamic effect becomes larger than the diffusive flux of adhesion to the wall. Elongated regions of high shear stress become



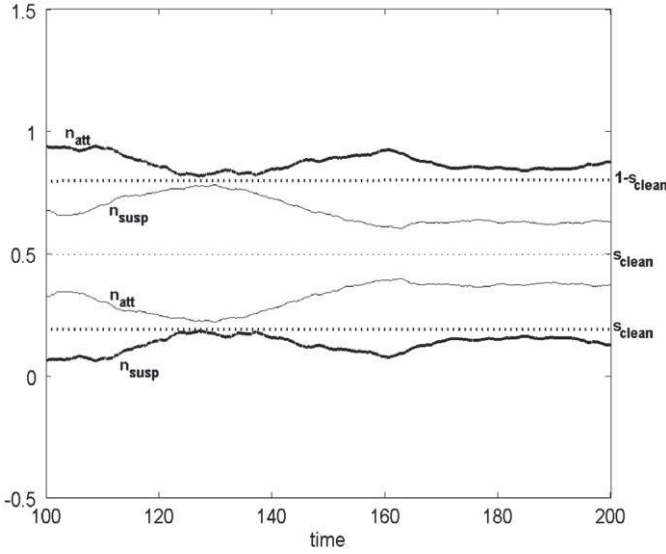


**Fig. 14.**  $n_{susp}$  and  $n_{att}$  versus time for  $s_{clean}=20\%$  (thicker lines,  $\tau_{crit}/\langle\tau_w\rangle=1.48$ ) and  $s_{clean}=50\%$  (thinner lines,  $\tau_{crit}/\langle\tau_w\rangle=0.91$ ). Dimensionless time:  $\langle\bar{u}\rangle t/h$ .

thicker (in the spanwise direction) when  $s_{clean}$  is increased and, thus, removal of attached particles is enhanced.

## 5. Conclusion

Direct simulation of particle transport in turbulent flow near a permeable surface was performed by coupling Lagrangian particle tracking to the full simulation of near-wall turbulent structures of the fluid flow. It allows simultaneous modeling of physical phenomena such as transport, deposition, detachment and re-entrainment of Brownian particles suspended in a turbulent channel flow experiencing cross-flow filtration. Results of fully coupled simulations demonstrate the possibility of using the model to predict the macroscopic behavior of the process but also to obtain insights into local and temporal hydrodynamic phenomena.

From a macroscopic point of view, these simulations show that turbulence deeply modifies particle mass flux near the permeable wall. We compared our averaged results to macroscopic prediction in the absence of particle detachment and we found good agreement. Statistical analysis of the temporal build-up of the concentration layer due to the permeation velocity allows adhesion and re-entrainment fluxes to be measured. These fluxes can be scaled into Sherwood numbers and have been compared to theoretical predictions adapted to turbulent flow conditions for the case of perfectly adhesive walls.

Furthermore, the present results show that under low turbulent conditions ( $Re=4000$ ) the presence of bursting, sweeping events and streaks (elongated coherent flow structure) leads to strong spatial and temporal fluctuations of the wall shear stress. The consequence of these instantaneous and local flow structures on the mechanism of particle adhesion and detachment from a permeable wall is discussed. The local formation of streaks changes the wall shear stress and the mass flux by the presence of a fluid ejection zone (high fluid velocity away from the wall) and of a fluid advection zone (high fluid velocities towards the wall). These streaks strongly modify the force balance acting on particles near the surface. The present study shows the role of these near-wall events on local deposition and re-entrainment fluxes in turbulent dilute particle dispersion channel flows in the absence of electric repulsion.

## Nomenclature

$c$	particle concentration (part/m <sup>3</sup> )
$C_L$	lift coefficient
$C_M$	added mass coefficient
$D=2h$	distance between channel walls (m)
$d_p$	particle diameter (m)
$D_p$	particle diffusivity (m <sup>2</sup> /s)
$\mathbf{F}$	force (N)
$F_D, F_L, F_A$	force of drag, lift, adhesion (N)
$g$	gravitational acceleration (m/s <sup>2</sup> )
$h$	half distance between two walls (m)
$k$	shear intensity (s <sup>-1</sup> )
$k_B$	Boltzmann constant, $1.381 \times 10^{-23}$ (J/K)
$K = -(\partial p / \partial x)$	opposite of the pressure gradient in the x direction (Pa/m)
$K_e$	reduced elastic modulus (Pa)
$l_1$	wall-attached particle center distance (m)
$l_2$	contact area radius (m)
$L$	particle distance from the wall (m)
$m$	mass (kg)
$\bar{M}_A$	moment of adhesion forces (N m)
$\bar{M}_D$	moment of surfaces stresses (N m)
$n_{susp}$	dimensionless suspended particle number
$n_{att}$	dimensionless attached particle number
$N_{tot}$	total number of particles
$N_{susp}$	total number of suspended particles
$N_{att}$	total number of attached particles
$P$	pressure (Pa)
$P(\text{hit})$	hit probability
$Pe$	Peclet number
$r_p$	particle radius (m)
$Re$	Reynolds number
$Re_\tau$	shear Reynolds number
$s_{clean}$	clean surface fraction (where detachment occurs)
$S$	wall surface (m <sup>2</sup> )
$Sc$	Schmidt number
$St$	Stokes number
$Sh$	Sherwood number
$t$	time (s)
$T$	temperature (K)
$u$	average fluid velocity in x-direction (m/s)
$u^+$	dimensionless velocity in wall units
$\mathbf{u}$	fluid velocity (m/s)
$u_w$	filtration velocity (m/s)
$u^*$	shear velocity (m/s)
$\mathbf{v}$	particle velocity (m/s)
$V$	volume (m <sup>3</sup> )
$x^+$	dimensionless x coordinate
$y^+$	distance from the wall in dimensionless wall units
$x, y, z$	spatial coordinates
$z^+$	dimensionless z coordinate

## Greek symbols

$\Phi$	particle flux per area (part/(s m <sup>2</sup> ))
$\delta_v$	thickness of the viscous sublayer (m)
$\delta_c$	thickness of the concentration boundary layer (m)
$\rho$	density (kg/m <sup>3</sup> )
$\mu, \nu$	fluid viscosity, dynamic and kinematic (kg/m s), (m <sup>2</sup> /s)
$\Delta t$	time step (s)
$\tau_f$	fluid flow time scale (s)
$\tau_p$	particle relaxation time (s)
$\tau_w$	wall shear stress (Pa)
$\omega$	vorticity (s <sup>-1</sup> )

$\omega_A$	work of adhesion (N m)
$\xi$	random number from a Gaussian distribution with zero mean and unity standard deviation

### Subscripts and Superscripts

+	dimensionless unit
o	initial value
att	attached
p	particle
sed	sedimentation
susp	suspended
tot	total
w	wall
<~>	average in space and time

### References

- Adomeit, P., Renz, U., 1996. Deposition of fine particles from a turbulent liquid flow, experiments and numerical predictions. *Chem. Eng. Sci.* 51, 3491–3503.
- Bacchin, P., Espinasse, B., Aimar, P., 2005. Distributions of critical flux: modelling, experimental analysis and consequences for cross-flow membrane filtration. *J. Membr. Sci.* 250 (1–2), 223–234.
- Bowen, B.D., Levine, S., Epstein, N., 1976. Fine particle deposition in laminar flow through parallel-plate and cylindrical channels. *J. Colloid Interface Sci.* 54, 375–390.
- Bowen, B.D., Epstein, N., 1979. Fine particle deposition in smooth parallel—plate channels. *J. Colloid Interface Sci.* 72, 81–97.
- Burdick, G.M., Berman, N.S., Beaudoin, S.P., 2001. Describing hydrodynamic particle removal from surfaces using the particle Reynolds number. *J. Nano-particle Res.* 3, 455–467.
- Calmet, I., Magnaudet, J., 1997. Large – eddy simulation of high – Schmidt number mass transfer in a turbulent channel flow. *Phys. Fluids* 9, 438–455.
- Calmet, I., Magnaudet, J., 2003. Statistical structure of high-Reynolds-number turbulence close to the free surface of an open-channel flow. *J. Fluid Mech.* 474, 355.
- Cleaver, J.W., Yates, B., 1975. A sub-layer model for the deposition of particles from a turbulent flow. *Chem. Eng. Sci.* 30, 983–992.
- Climent, E., Magnaudet, J., 2006. Dynamics of a two-dimensional upflowing mixing layer seeded with bubbles: bubble dispersion and effect of two-way coupling. *Phys. Fluids* 18, 103304.
- Dabros, T., Van de Ven, T.G.M., 1983. On the convective diffusion of fine particles in turbulent flow. *J. Colloid Interface Sci.* 92, 403–415.
- Davies, C.N., 1966. Deposition from moving Aerosol. *Aerosol Science*. Academic Press, London.
- Fuchs, N.A., 1964. *The Mechanics of Aerosols*. Pergamon Press, Oxford, pp. 195–197.
- Hanh, S., Je, J., Choi, H., 2002. Direct numerical simulation of turbulent channel flow with permeable walls. *J. Fluid Mech.* 450, 259–285.
- Israelachvili, J., 1991. *Intermolecular and Surfaces Forces*, second edition Academic Press.
- Jeong, J., Hussain, F., Schoppa, W., Kim, J., 1997. Coherent structures near the wall in a turbulent channel flow. *J. Fluid Mech.* 332, 185–214.
- Johnson, K.L., Kendall, K., Roberts, A.D., 1971. Surface energy and the contact of elastic solids. *Proc. R. Soc. London* 324, 301–313.
- Kim, M.M., Zydney, A.L., 2004. Effect of electrostatic, hydrodynamic, and Brownian forces on particle trajectories and sieving in normal flow filtration. *J. Colloid Interface Sci.* 269, 425–431.
- Kloeden, P.E., Platen, E., 1992. *Numerical Solution of Stochastic Differential Equations*. Springer-Verlag, Berlin Heidelberg, pp. 501–510.
- Kreplin, H.P., Eckelman, H., 1979. Behavior of the three fluctuating velocity components in the wall region of a turbulent channel flow. *Phys. Fluids* 22 (7), 1233.
- Lai, A.C.K., Nazaroff, W.W., 2000. Modelling indoor particle deposition from turbulent chamber flow onto smooth surfaces. *J. Aerosol Sci.* 31, 463–476.
- Li, H., Fane, A.G., Coster, H.G.L., Vigneswaran, S., 2003. Observation of deposition and removal behaviour of submicron bacteria on the membrane surface during crossflow microfiltration. *J. Membr. Sci.* 217, 29–41.
- Magnaudet, J., Rivero, M., Fabre, J., 1995. Accelerated flows past a rigid sphere or a spherical bubble. Part I: steady straining flow. *J. Fluid Mech.* 284, 97–135.
- Maniero, R., Canu, P., 2006. A model of fine particles deposition on smooth surfaces – I – theoretical basis and model development. *Chem. Eng. Sci.* 61, 7626–7635.
- Maniero, R., Canu, P., 2007. A model of fine particles deposition on smooth surfaces – II – validation against experimental data and simplified models. *Chem. Eng. Sci.* 62, 2821–2832.
- Mannella, R., 1999. Absorbing boundaries and optimal stopping in a stochastic differential equation. *Phys. Lett. A* 254, 257–262.
- Marchioli, C., Giusti, A., Salvetti, M.V., Soldati, A., 2003. Direct numerical simulation of particle wall transfer and deposition in upward turbulent pipe flow. *Int. J. Multiphase Flow* 29, 1017–1038.
- Minnikanti, V.S., DasGupta, S., De, S., 1999. Prediction of mass transfer coefficient with suction for turbulent flow in cross flow ultrafiltration. *J. Membr. Sci.* 157, 227–239.
- Moin, P., Kim, J., 1982. Numerical investigation of turbulent channel flow. *J. Fluid Mech.* 118, 341–377.
- Negri, F., Bedel, E., Schmitz, P., 2002. Experimental study of alumina particle removal from a plane surface. *J. Adhes.* 78, 79–95.
- Rajae, M., Karlsson, S., Sirovich, L., 1995. On the streak spacing and vortex roll size in a turbulent channel flow. *Phys. Fluids* 7 (10), 2439.
- Rouson, D.W.I., Eaton, J.K., 2001. On the preferential concentration of solid particles in turbulent channel flow. *J. Fluid Mech.* 428, 149–169.
- Russel, W.B., Saville, D.A., Schowalter, W.R., 1989. *Colloidal Dispersions*. Cambridge University Press, Cambridge, pp. 153–156.
- Sehmel, G.A., 1970. Particle deposition from turbulent air flow. *J. Geophys. Res.* 75, 1766–1781.
- Shams, M., Ahmadi, G., Rahimzadeh, H., 2000. A sublayer model for deposition of nano- and micro-particles in turbulent flows. *Chem. Eng. Sci.* 55, 6097–6107.
- Sheng, J., Malkiel, E., Katz, J., 2009. Buffer layer structures associated with extreme wall stress events in a smooth wall turbulent boundary layer. *J. Fluid Mech.* 633, 17–60.
- Song, L., Elimelech, M., 1995. Particle deposition onto a permeable surface in laminar flow. *J. Colloid Interface Sci.* 173, 165–180.
- Spurk, J.H., 1997. *Fluid Mechanics (Problems and Solutions)*. Springer, ISBN: 3-540-61652-7.
- Xu, J., Maxey, M.R., Karniadakis, G.E., 2002. Numerical simulation of turbulent drag reduction using micro-bubbles. *J. Fluid Mech.* 468, 271–281.
- Yiantsios, S.G., Karabelas, A.J., 1995. Detachment of spherical microparticles adhering on flat surfaces by hydrodynamic forces. *J. Colloid Interface Sci.* 176, 74–85.
- Yiantsios, S.G., Karabelas, A.J., 2003. Deposition of micron-sized particles on flat surfaces: effects of hydrodynamic and physicochemical conditions on particle attachment efficiency. *Chem. Eng. Sci.* 58, 3105–3113.
- Yung, P.K., Merry, H., Bott, T.R., 1989. The role of turbulent burst in particle re-entrainment in aqueous systems. *Chem. Eng. Sci.* 44, 873–882.
- Zhang, H., Ahmadi, G., 2000. Aerosol particle removal and re-entrainment in turbulent channel flows—a direct numerical simulation approach. *J. Adhes.* 74, 441–493.
- Ziskind, G., Fichman, M., Gutfinger, C., 1995. Resuspension of particulates from surfaces to turbulent flows—review and analysis. *J. Aerosol Sci.* 25 (4), 613–644.
- Ziskind, G., Fichman, M., Gutfinger, C., 1997. Adhesion moment model for estimating particle detachment from a surface. *J. Aerosol Sci.* 28 (4), 623–634.